Mon. Not. R. Astron. Soc. **000**, 1–16 (2014) Printed 3 March 2014 (MN LATEX style file v2.2)

Cold dark matter haloes in the Planck era: evolution of structural parameters for Einasto and NFW profiles

Aaron A. Dutton⋆, Andrea V. Macciò
Max-Planck-Institut für Astronomie, Königstuhl 17, 69117 Heidelberg, Germany

arXiv:1402.7073v1 [astro-ph.CO] 27 Feb 2014

submitted to MNRAS

ABSTRACT

We present the evolution of the structure of relaxed cold dark matter haloes in the cosmology from the Planck satellite. Our simulations cover 5 decades in halo mass, from dwarf galaxies to galaxy clusters. Due to the increased matter density and power spectrum normalization the concentration mass relation in the Planck cosmology has a $\sim 20\%$ higher normalization at redshift $z = 0$ compared to WMAP cosmology. We confirm that CDM haloes are better described by the Einasto profile; for example, at scales near galaxy half-light radii CDM haloes have significantly steeper density profiles than implied by NFW fits. There is a scatter of ~ 0.2 dex in the Einasto shape parameter at fixed halo mass, adding further to the diversity of CDM halo profiles. The evolution of the concentration mass relation in our simulations is not reproduced by any of the analytic models in the literature. We thus provide a simple fitting formula that accurately describes the evolution between redshifts $z = 5$ to $z = 0$ for both NFW and Einasto fits. Finally, the observed concentrations and halo masses at low redshifts of spiral galaxies, groups and clusters of galaxies are in good agreement with our simulations, suggesting only mild halo response on these scales.

Key words: galaxies: haloes – cosmology:theory, dark matter – methods: numerical

1 INTRODUCTION

In the standard theoretical framework for structure formation in the Universe, the mass-energy budget is dominated by a cosmological constant and cold dark matter (CDM). In this paradigm, initially small density perturbations grow via gravitational instability, forming bound structures known as dark matter haloes.

The structure of dark matter haloes are of particular interest as they provide a non-linear scale test of the cold dark matter paradigm, cosmological parameters, and more generally for the nature of dark matter itself (e.g., Moore 1994; Flores & Primack 1994; de Blok et al. 2001; Zentner & Bullock 2002; McGaugh 2004). They also provide the backbone for the structural properties of galaxies and galaxy scaling relations (e.g., Mo et al. 1998; Dutton et al. 2007).

From the theoretical side there are two hurdles that need to be overcome before an accurate prediction for the structure of CDM haloes is possible: 1) halo structure is sensitive to cosmological parameters (e.g., Macciò et al. 2008) and 2) the galaxy formation process can cause haloes to both contract or expand (e.g., Di Cintio et al. 2014). The subject of this paper is to constrain the effects of the cosmological parameters on the "baryon free" dark halo structure, and to quantify the evolution of the structure of CDM haloes as a population across cosmic time. This work continues on from our earlier studies (Macciò et al. 2007, 2008; Muñoz-Cuartas et al. 2011), as well as numerous studies in the literature (e.g., Navarro, Frenk & White 1996, 1997; Bullock et al. 2001; Eke et al. 2001; Zhao et al. 2003, 2009; Duffy et al. 2008; Gao et al. 2008; Klypin et al. 2011; Prada et al. 2012; Ludlow et al. 2013).

As shown by Macciò et al. (2008) relatively small changes in cosmological parameters have a non-negligible effect on the structure of dark matter haloes. For example, the mean concentrations of dark matter haloes varied by a factor of 1.5 between the various WMAP cosmologies (Spergel et al. 2003, 2007). The cosmology advocated by the Planck satellite (the Planck Collaboration 2013) has a significantly higher matter density, $\Omega_{\rm m}$, than adopted in all previous high-resolution simulations (See Fig. 1 and Table 1). Compared to the WMAP 5th year cosmology (Komatsu et al. 2009), the Planck cosmology also has higher σ_8. These differences are expected to result in increased dark halo concentrations (e.g., using the model of Bullock et al. 2001).

Traditionally the structure of CDM haloes has been described by the two parameter NFW profile (Navarro, Frenk, & White 1996; 1997). This has a divergent inner density

⋆ dutton@mpia.de

© 2014 RAS

Table 1. Cosmological Parameters. All cosmologies are flat, i.e., $\Omega_\Lambda + \Omega_\mathrm{m} = 1$.

Name	Ω_m	h	σ_8	n	Ω_b	Simulation Reference
Planck	0.3175	0.671	0.8344	0.9624	0.0490	This paper
WMAP5	0.258	0.72	0.796	0.963	0.0438	Macciò et al. 2008
WMAP3	0.238	0.73	0.75	0.95	0.042	Macciò et al. 2008
WMAP1	0.268	0.71	0.90	1.0	0.044	Macciò et al. 2008
Millennium	0.25	0.73	0.90	1.0	0.045	Springel et al. 2005
Bolshoi	0.27	0.70	0.82	0.95	0.0469	Klypin et al. 2011

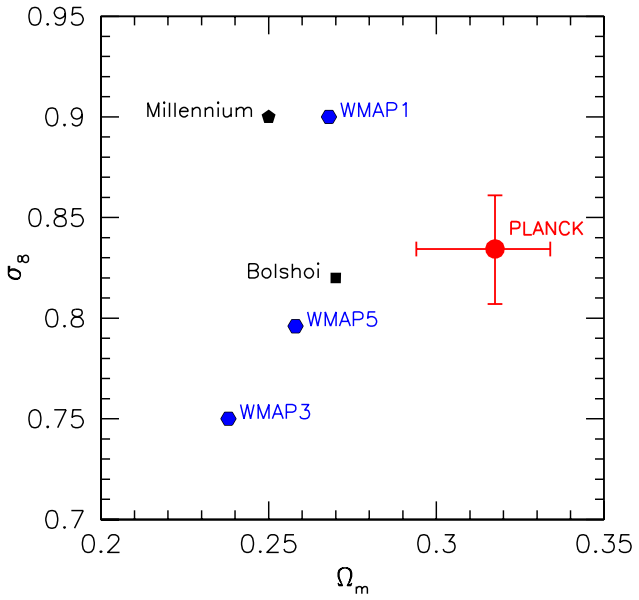

Figure 1. Constraints on the cosmic matter density (Ω_m) and the power spectrum normalization (σ_8) from the Planck Collaboration (2013) (red point with 68% confidence interval). For comparison, the various sets of cosmological parameters from the WMAP satellite are shown with blue hexagons (1st, 3rd and 5th year results), and the parameters used by the Millennium and Bolshoi N-body simulations are given by the black pentagon and square, respectively.

profile of $\rho(r) \propto r^{-1}$, and an outer profile of $\rho(r) \propto r^{-3}$. A common parametrization uses the halo mass, M_{200}, and the concentration parameter, $c \equiv R_{200}/r_{-2}$ (where R_{200} is the virial radius, and r_{-2} is the scale radius). The mass and concentration are correlated, with a shallow slope ($c \propto M_{200}^{-0.1}$), and small scatter ($\sigma_{\log c} \sim 0.1$), so the structure of CDM haloes is almost scale free and described by a universal profile (NFW 97; Bullock et al. 2001).

Recent work has shown that three parameters provide a more accurate description of spherically average cold dark matter density profiles - especially at small radii ($\sim 1\%$ of the virial radius). The most common generalizations are to allow the inner logarithmic density slope, γ, to be a free parameter (recall the NFW profile has $\gamma = -1$), sometimes known as a generalized NFW profile (or gNFW); or the Einasto profile (Einasto 1965), which is $d\ln\rho/d\ln r \propto r^\alpha$. A number of studies have shown that the Einasto profile provides, in general, a better description of CDM haloes than the NFW or gNFW profiles (e.g., Navarro et al. 2004, 2010; Merritt et al. 2005, 2006; Stadel et al. 2009; Reed et al. 2011). Going one step further, using stacks of CDM haloes, Gao et al. (2008) showed that the Einasto shape parameter, α, depends on halo mass.

As in our earlier studies we use a large suite of cosmological N-body simulations with different box sizes to cover the entire halo mass range from $\sim 10^{10} h^{-1}\,\mathrm{M}_\odot$ (haloes that host dwarf galaxies) to $\sim 10^{15} h^{-1}\,\mathrm{M}_\odot$ (massive clusters). We use these simulations to investigate the structure of dark matter haloes across cosmic time. In estimating halo concentrations we consider fits to the density profiles using both the Einasto and NFW functions, as well as a non-parametric approximation utilizing V_max/V_{200} following Klypin et al. (2011).

This paper is organized as follows: in §2 the simulations and the determination of the halo parameters are presented. In §3 we discuss the quality of Einasto vs NFW fits as well as different methods for measuring halo concentrations. In §4 we compare the concentration mass relation of Planck cosmology to that from WMAP, and discuss the effects of different cosmological parameters. In §5 we present the evolution of the NFW concentration mass relation, while in §6, we present the evolution of the Einasto concentration and shape parameters. In §7 we compare the concentration mass relation from our simulations with observations of spiral galaxies and clusters of galaxies. Finally, we summarize our results in §8.

2 N-BODY SIMULATIONS

Table 2 lists the parameters of the simulations run in the Planck cosmology that are used in this paper. Our simulation set up and N-body methods follows closely that of Macciò et al. (2007; 2008). We ran simulations in eight different box sizes, which allows us to probe halo masses covering the range $10^{10}\mathrm{M}_\odot \lesssim M \lesssim 10^{15} h^{-1}\,\mathrm{M}_\odot$. Each simulation has a unique name, which refers to the box size in h^{-1}Mpc. In addition, in some case we have run multiple (up to four) simulations for the same box size in order to increase the final number of dark matter haloes and reduce any impact of cosmic variance.

All simulations have been performed with PKDGRAV, a tree code written by Joachim Stadel and Thomas Quinn (Stadel 2001). The code uses spline kernel softening, for which the forces become completely Newtonian at 2 softening lengths. Individual time steps for each particle are chosen proportional to the square root of the softening length, ϵ, over the acceleration, a: $\Delta t_\mathrm{i} = \eta\sqrt{\epsilon/a_\mathrm{i}}$. Throughout, we set $\eta = 0.2$, and we keep the value of the softening length constant in co-moving coordinates during each run. The physical values of ϵ at $z = 0$ are listed in Table 2. Forces are

Table 2. N-body simulation parameters for Planck cosmology runs.

Name	Box size $[h^{-1}\mathrm{Mpc}]$	N	part. mass $[h^{-1}\mathrm{M}_\odot]$	force soft. $[h^{-1}\mathrm{kpc}]$
P-20.1	20	300^3	2.611×10^7	1.67
P-20.2	20	300^3	2.611×10^7	1.67
P-20.3	20	300^3	2.611×10^7	1.67
P-20.4	20	300^3	2.611×10^7	1.67
P-30.1	30	300^3	8.811×10^7	2.50
P-30.2	30	300^3	8.811×10^7	2.50
P-60	60	600^3	8.811×10^7	2.50
P-45.1	45	300^3	2.974×10^8	3.75
P-45.2	45	300^3	2.974×10^8	3.75
P-90	90	450^3	7.049×10^8	5.00
P-80	80	350^3	1.052×10^9	5.71
P-130	130	450^3	2.124×10^9	7.22
P-180	180	450^3	5.639×10^9	10.0
P-270	270	450^3	1.903×10^{10}	15.0
P-400	400	450^3	6.188×10^{10}	22.2
P-600	600	600^3	8.811×10^{10}	25.0
P-1000	1000	600^3	4.079×10^{11}	41.7

computed using terms up to hexadecapole order and a node-opening angle θ which we change from 0.55 initially to 0.7 at $z = 2$. This allows a higher force accuracy when the mass distribution is nearly smooth and the relative force errors can be large. The initial conditions are generated with the GRAFIC2 package (Bertschinger 2001). The starting redshifts z_i are set to the time when the standard deviation of the smallest density fluctuations resolved within the simulation box reaches 0.2 (the smallest scale resolved within the initial conditions is defined as twice the intra-particle distance).

2.1 Halo catalog

In all simulations, dark matter haloes are identified using a spherical overdensity (SO) algorithm. Candidate groups with a minimum of $N_\mathrm{f} = 250$ particles are selected using a FoF algorithm with linking length $\phi = 0.2 \times d$ (the average particle separation). We then: (i) find the point C where the gravitational potential is minimum; (ii) determine the radius $\bar{r}$ of a sphere centered on C, where the density contrast is $\Delta(z)$, with respect to the *critical density* of the Universe, $\rho_\mathrm{crit}(z) = 3H(z)^2/8\pi G$. Using all particles in the corresponding sphere we iterate the above procedure until we converge onto a stable particle set. For each stable particle set we obtain the virial radius, R_vir, the number of particles within the virial radius, N_vir, and the virial mass, M_vir. For the Planck cosmology $\Delta(0) \simeq 104.2$, based on the fitting function of Mainini et al. (2003). Values of $\Delta(z)$ at other redshifts are given in Table 3. It is also convenient to define a virial radius, r_{200}, inside of which the density of the dark matter halo is 200 times ρ_crit; accordingly we also define M_{200} and N_{200} as the mass and the number of particles within r_{200}. The advantage of this definition is that the halo mass is independent of cosmology, i.e., for a given density profile the corresponding M_{200} is independent of cosmological parameters, whereas M_vir depends on $\Omega_\mathrm{m}(z)$. In the combined set of simulations there are 92 903 haloes with $N_\mathrm{vir} > 500$ at redshift $z = 0$. At $z = 0.5, 1, 2, 3, 4,$ & 5 the corresponding numbers are 77 824, 64 100, 42 001, 25 694, 14 064, and 7 061.

2.2 Density profile fitting

For each SO halo in our sample we determine a set of parameters, including the virial mass and radius, the maximum circular velocity and the concentration parameter. To compute the concentration of a halo we first determine its density profile. The halo center is defined as the location of the most bound halo particle. We compute the density (ρ_i) in 50 spherical shells, spaced equally in logarithmic radius. The minimum radius is either 1% of R_vir or 3 times the softening length (which ever is larger) and the maximum radius is $1.2R_\mathrm{vir}$. Errors on the density are computed from the Poisson noise due to the finite number of particles in each mass shell. We fit the density profiles with two different formulae. The NFW profile (Navarro et al. 1997), and the Einasto profile (Einasto 1965).

The NFW profile is given by

$$\frac{\rho_\mathrm{NFW}(r)}{\rho_{-2}} = \frac{4}{(r/r_{-2})(1+r/r_{-2})^2}, \tag{1}$$

where r_{-2} is the radius where the logarithmic slope of the density profile is -2 (also known as the scale radius), and ρ_{-2} is the density at the scale radius. During the fitting procedure we treat both r_{-2} and ρ_{-2} as free parameters. Their values, and associated uncertainties, are obtained via a χ^2 minimization procedure using the Levenberg & Marquart method. We define the r.m.s. of the fit as:

$$\rho_\mathrm{rms} = \frac{1}{N}\sum_i^N (\ln\rho_i - \ln\rho_\mathrm{m})^2 \tag{2}$$

where ρ_m is the fitted NFW density distribution. The Einasto profile (Einasto 1965) has an extra free parameter, α, and is given by

$$\frac{\rho_\mathrm{EIN}(r)}{\rho_{-2}} = \exp\left\{-\frac{2}{\alpha}\left[(r/r_{-2})^\alpha - 1\right]\right\}. \tag{3}$$

The concentration of the halo is defined as, $c_\mathrm{vir} \equiv R_\mathrm{vir}/r_{-2}$, or $c_{200} \equiv R_{200}/r_{-2}$. Where the virial radius (either R_vir or R_{200}) is obtained from the SO algorithm, and the scale radius is obtained from the density profile fits. We define the error on $\log c$ as $(\sigma_{r_{-2}}/r_{-2})/\ln(10)$, where σ_r is the fitting uncertainty on r_{-2}.

An alternative means of estimating the concentration of the dark matter halo utilizes the maximum circular velocity of the halo, V_max. The circular velocity for a spherical mass distribution is given by $V(r) = \sqrt{GM(r)/r}$. For the NFW and Einasto profiles there is a monotonic relation between V_max/V_{200} and the concentration parameter, and thus V_max/V_{200} can be used to obtain an *estimate* for the concentration without explicitly fitting the density profile. This method has been used by Klypin et al. (2011) and Prada et al. (2012), who discovered a surprising upturn in the concentration mass relation at high masses and redshifts.

For our simulated haloes we calculate V_max using the same radial grid which we use for the density profile, and we calculate the concentration assuming the NFW relation between V_max/V_{200} and halo concentration:

$$V_\mathrm{max}/V_{200} \simeq \sqrt{0.216\, c_{200}/f(c_{200})}, \tag{4}$$

where $f(c)$ is

$$f(c) = \ln(1+c) - c/(1+c). \quad (5)$$

An important caveat in this calculation is that the relation between concentration and $V_{\rm max}/V_{200}$ depends on the Einasto shape parameter, α. While for typical ΛCDM halo concentrations the Einasto profile with $\alpha = 0.2$ results in very similar concentrations as that of the NFW profile (Prada et al. 2012), ΛCDM haloes in general have $\alpha \neq 0.2$. It is known (e.g., Gao et al. 2008) and we also show below in §6, that the average α increases with halo mass and redshift. Higher/lower values of α will result in higher/lower $V_{\rm max}/V_{200}$, and hence higher/lower concentrations when assuming the NFW relation. A value of $\alpha = 0.2$ is typical for galaxy cluster haloes at redshift $z = 0$, and Milky Way mass haloes at $z = 3$. Thus we expect the $V_{\rm max}/V_{200}$ method to underestimate halo concentrations at low redshift and overestimate them in massive haloes at high-redshift. These expectations are realized in §3.1. Additionally, $V_{\rm max}$ is sensitive to transient features due to unrelaxed haloes which result in an over-estimate of the true concentration (Ludlow et al. 2012).

2.3 Relaxed Haloes

Our halo finder (and halo finders in general) does not distinguish between relaxed and unrelaxed haloes. Unrelaxed haloes often have poorly defined centers, which makes the determination of a radial density profile, and hence of the concentration parameter, an ill-defined problem. Following Macciò et al. (2007; 2008) we select relaxed haloes with the condition $\rho_{\rm rms} < 0.5$ and $x_{\rm off} < 0.07$. Here $\rho_{\rm rms}$ is the r.m.s. of the NFW fit to the density profile and $x_{\rm off}$ is the offset between the most bound particle and the center of mass, in units of the virial radius $R_{\rm vir}$. This offset is a measure of the dynamical state of the halo: relaxed haloes in equilibrium will have a smooth, radially symmetric density distribution, and thus an offset parameter that is virtually equal to zero. Unrelaxed haloes, such as those that have only recently experienced a major merger, are likely to have a strongly asymmetric mass distribution, and thus a relatively large $x_{\rm off}$. At redshift $z = 0$ about 80% of the haloes in our sample qualify as relaxed haloes. This number decreases towards higher redshifts, reaching $\sim 50\%$ at redshift $z = 5$.

2.4 Resolution considerations

In this section we address the issue of the minimum number of particles, $N_{\rm min}$, needed to measure reliable halo concentrations. We consider both an empirical determination (i.e., convergence of the concentration mass relation for different $N_{\rm min}$), and physically motivated arguments on the ability to resolve the scale radius.

The softening length sets a minimum scale within which the enclosed masses are not reliable (the actual resolved scale may be larger than this). In our simulations the softening length is set to be $\epsilon = 0.025L/N$ in co-moving coordinates, where L is the box size and N^3 is the number of particles. Since the particle mass is given by $m_{\rm p}/[h^{-1}\,{\rm M}_\odot] = 2.775\times10^{11}({\rm L}/[{\rm h}^{-1}{\rm Mpc}])^3{\rm N}^{-3}\Omega_{\rm m}$, the minimum halo mass by $M_{\rm min} = N_{\rm min}m_{\rm p}$ and $R_{\rm min} = (GM_{\rm min})^{1/3}$, we get

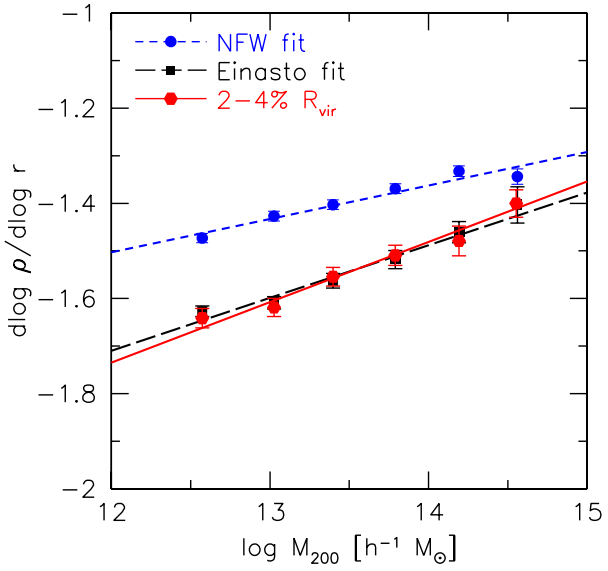

Figure 2. Logarithmic density slope at 3% of the virial radius for relaxed haloes with more than 63,000 particles. Results from a direct fit from 2 to 4% of the viriral radius are given in red. Results from NFW and Einasto fits to the density profiles are given in blue and black, respectively. Simulated haloes are thus significantly steeper than the NFW function, but in excellent agreement with the Einasto function.

an estimate for the maximum concentration measurable as a function of the minimum number of particles per halo $R_{\rm min}/\epsilon = 29.0(N_{\rm min}/1000)^{1/3}$. Since typical halo concentrations at redshift zero are ~ 10, this would suggest a few hundred particles could be sufficient to resolve the scale radius. Such a conclusion is backed up by our empirical convergence studies of the concentration mass relation (see also Macciò et al. 2007). For this study we adopt $N_{\rm min} = 500$ when using NFW fits which is the same as adopted by comparable studies (e.g., Klypin et al. 2011).

Since the Einasto profile has an extra free parameter there are more degeneracies than when fitting the NFW profile. In particular, for poorly resolved haloes there is a strong degeneracy between α and c. As such, one would expect that more particles are needed in order to obtain reliable Einasto scale radii and shape parameters. These expectations are realized in our empirical convergence tests of the concentration mass relation. For Einasto fits we require several thousand particles per halo, with more particles at lower redshifts. The redshift dependence is expected since halo concentrations are, on average, higher at lower redshifts, and more particles are formally required to resolve the scale radii in haloes with higher concentrations. At redshift $z = 0$ in the order of 10 000 particles per halo are needed.

Power et al. (2003) give a number of convergence criteria for N-body simulations. For our purposes the strictest requirement is the relaxation time (Eq. 20 in Power et al. 2003). For resolving the scale radius, this can be approximated with $N_{\rm min} = 16000(c_{200}/10)^2$. A strict application of this criteria would result in a bias against high concentrations at masses near the resolution limit. To get around this we select the minimum halo mass such that 84%

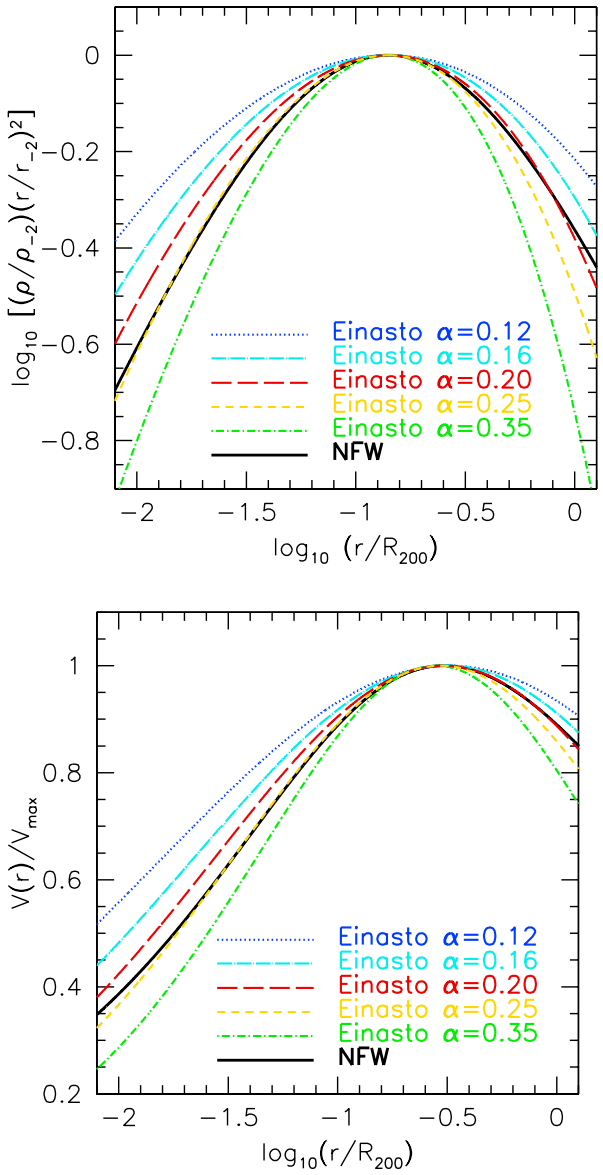

Figure 3. Einasto vs NFW density and circular velocity profiles for typical Einasto shape parameters (α) found in CDM haloes. Note that at small radii ($0.01 \lesssim R/R_{200} \lesssim 0.1$) the Einasto profile with $\alpha = 0.25$ is very similar to the NFW profile, while for large radii ($0.1 \lesssim R/R_{200} \lesssim 1$) the Einasto profile with $\alpha = 0.2$ is most similar to the NFW profile.

of the haloes at that mass satisfy the resolution requirement. This is given by

$$N_{\rm min}(M_{200}, z) = 16000[1.29\bar{c}_{200}(M_{200}, z)/10]^2, \quad (6)$$

where $\bar{c}_{200}(M_{200})$ is obtained from our empirical fits to the evolution of the concentration mass relation (see below). In addition to Eq. 6 we impose $N_{\rm min} = 3000$ for Einasto fits. Our minimum particle numbers are thus at least as strict as used by other authors employing Einasto fits: Gao et al. (2008) who set $N_{\rm min} = 3000$, and Ludlow et al. (2013) who set $N_{\rm min} = 5000$.

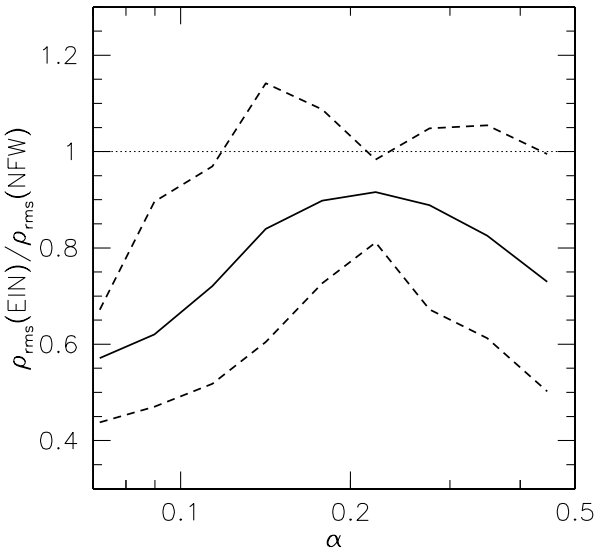

Figure 4. Ratio between the root mean square of deviations in $\ln\rho$ between simulated density profiles and analytic fits using the Einasto and NFW profiles. The solid line shows the median, while the dashed lines show the 16th and 84th percentiles. The majority of haloes have $\rho_{\rm rms}({\rm EIN})/\rho_{\rm rms}({\rm NFW}) < 1$ indicating the Einasto profile provides better fits for all values of the Einasto shape parameter, α. Note there is a minimum in scatter at $\alpha \sim 0.2$, which is due to the similarity between the NFW and Einasto profiles over the typical radii resolved in our simulations.

3 EINASTO VS NFW

Fig. 2 shows a comparison between the logarithmic density slopes of our simulated haloes at three percent of the virial radius computed using three different methods. Only haloes with more than 63 000 particles are considered here, to ensure the profiles are fully resolved at this scale. The black squares show the average slope calculated using Einasto fits to the whole profile, the blue squares show the corresponding slopes for NFW fits, while the red circles show the slopes from a direct power-law fit to the density profile between 2 and 4% of the virial radius. This shows that simulated haloes have steeper inner slopes than the NFW fits would suggest, but in excellent agreement with the Einasto profile. This result agrees with previous studies at lower (Navarro et al. 2010) and higher masses (Reed et al. 2011).

A comparison between the Einasto and NFW profiles is shown in Fig. 3. The upper panel shows the density profile, while the lower panel shows the circular velocity profile. The NFW profile is shown with a solid black line, while the Einasto profiles with $\alpha = 0.12, 0.16, 0.20, 0.25$, and 0.35 are shown with colored lines as indicated. These values of α are chosen to bracket the typical range for CDM haloes. This figure shows that at large radii ($> r_{-2}$) $\alpha \simeq 0.2$ provides a good match to the NFW profile. However, for radii less than 10% of the virial radius, $\alpha \simeq 0.2$ results in higher densities and circular velocities than the NFW profile. A very good match between NFW and Einasto for 1 to 10% of the virial radius is achieved with $\alpha = 0.25$. As shown below such values of α occur for high$-\sigma$ haloes (See also Gao et al. 2008).

Fig. 4 shows a comparison of the root mean square de-

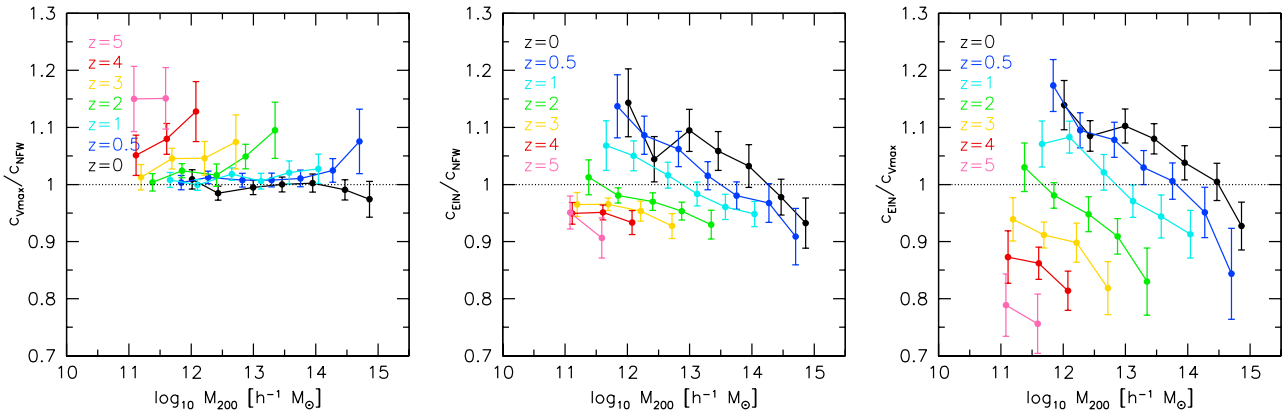

Figure 5. Dependence of halo concentrations on fitting procedure. Different colors represent different redshifts from $z = 0$ to $z = 5$ as indicated. Left: ratio of concentrations from $V_{\rm max}/V_{200}$ and NFW fits. Middle: Ratio of concentrations from Einasto and NFW fits; Right: Ratio of concentrations from Einasto fits and $V_{\rm max}/V_{200}$. The differences in concentrations can be as large as 20%

viations of $\ln \rho$ for Einasto and NFW fits at redshift $z = 0$ (similar results are present at other redshifts). This shows that for all values of the Einasto shape parameter, α, the majority of simulated haloes are better fit with an Einasto profile than an NFW profile. Interestingly, as might be expected from Fig. 3, the NFW fits come closest to the Einasto fits for $\alpha \sim 0.2$, since this is where the Einasto and NFW profiles are most similar for typical fitting regions ($0.1 \lesssim r/R_{200} \lesssim 1$).

3.1 Comparison between concentration estimates

In this paper we consider three different measurements of the halo concentration: NFW fits to the density profile ($c_{\rm NFW}$), Einasto fits to the density profile ($c_{\rm EIN}$), and the $V_{\rm max}/V_{200}$ ratio assuming an NFW profile ($c_{V_{\rm max}}$). In Fig. 5 we show the ratio between two concentration estimates, for the three combinations: $c_{V_{\rm max}}/c_{\rm NFW}$ (left); $c_{\rm EIN}/c_{\rm NFW}$ (middle); and $c_{V_{\rm max}}/c_{\rm EIN}$ (right). The symbols show the median while the error bars show the statistical uncertainty on the median. Since the halo radii are the same for each method the concentration ratio is equivalent to the ratio of the scale radii. In order to compare all concentrations equally we use the stricter Einasto fit particle number requirements.

3.1.1 $V_{\rm max}$ vs NFW

At redshift zero the NFW and $V_{\rm max}$ methods give very similar results, the differences are consistent with statistical uncertainties. However, at higher redshifts and especially higher masses, the $V_{\rm max}$ method gives systematically higher concentrations, up to 15%. These results are consistent with the tests from Prada et al. (2012) (see their Figure 4), which show the $V_{\rm max}$ method gives higher concentrations than NFW fits, especially for low concentration haloes.

Since any perturbations from a NFW profile (either from real features or statistical uncertainties) will preferentially scatter $V_{\rm max}$ up. Additionally, for lower concentrations the velocity ratio approaches unity ($V_{\rm max}/V_{200} = 1$ for $c_{200} \simeq 2.2$), and thus errors in the velocity ratio propagate into larger uncertainties in concentrations. Since halo concentrations are lower at higher masses and redshifts, any systematic effects are amplified.

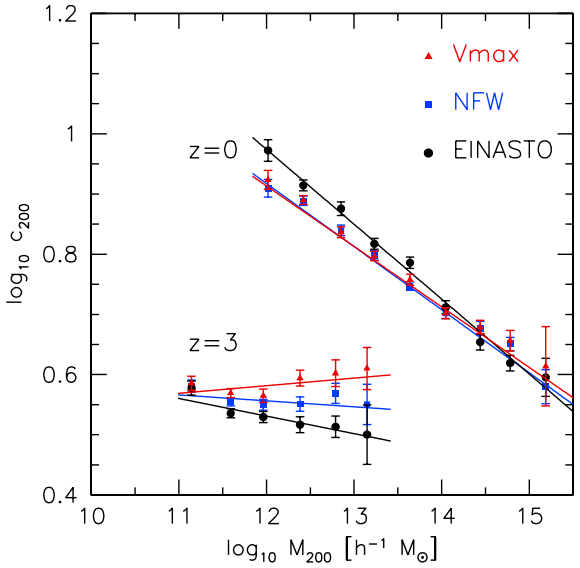

Figure 6. Dependence of the halo concentration mass relation on fitting procedure. The colors and point types indicate the different methods: Einasto fits (black circles); NFW fits (blue squares); $V_{\rm max}/V_{200}$ (red triangles). Notice that the Einasto fits give a steeper slope to the concentration mass relation at redshift $z = 0$, while the $V_{\rm max}$ method gives a positive slope to the concentration mass relation at redshift $z = 3$.

3.1.2 NFW vs Einasto

The deviations between NFW and Einasto concentrations are within $\sim 15\%$ at all redshifts. There is a clear trend between the concentration ratio and halo mass, which translates into steeper slopes for the Einasto concentration mass relation, as well as stronger evolution (Fig. 6, and §'s 5 & 6). These trends are qualitatively consistent with the mass and redshift dependence of the Einasto shape parameter.

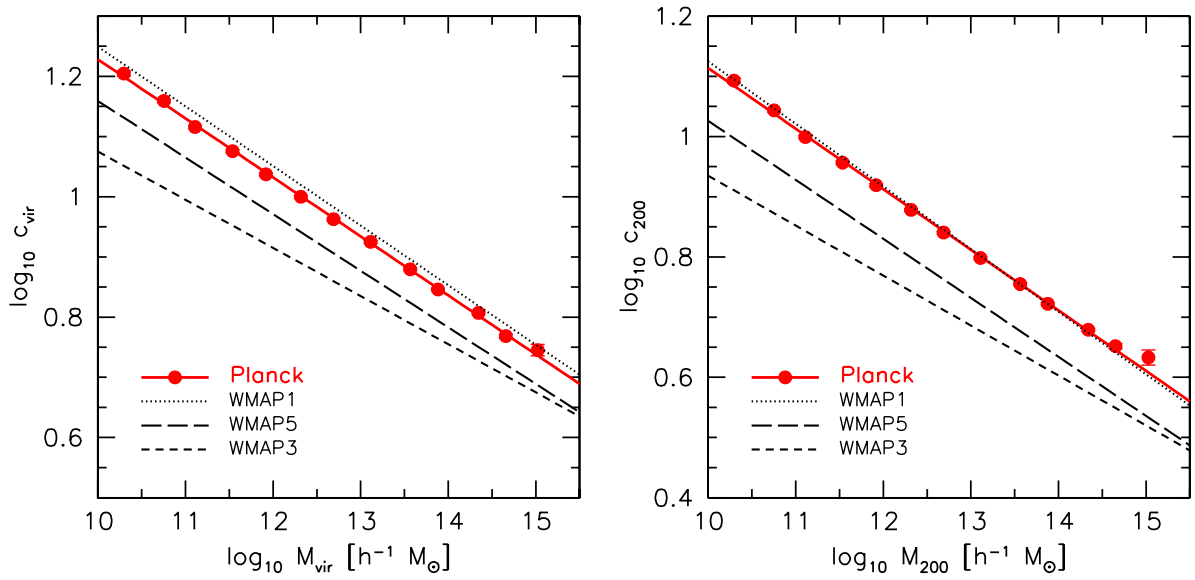

Figure 7. Concentration mass relations for the Planck cosmology (red circles), for the "virial" (left) and $200\rho_{\rm crit}$ (right) definitions of halo masses and sizes. Power-law fits are shown with red lines. For comparison, fits to the relations for WMAP cosmologies from Macciò et al. (2008) are shown with black lines: WMAP1 (dotted), WMAP3 (short dashed), and WMAP5 (long-dashed). The concentration mass relation for the Planck cosmology is remarkably similar to that from WMAP1, inspite of the different cosmological parameters (see Table 1). Note that with the "virial" halo definition the over density of the halo with respect to the critical density depends on $\Omega_{\rm m}$, and thus varies between cosmologies.

3.1.3 $V_{\rm max}$ vs Einasto

The $V_{\rm max}$ and Einasto concentrations show the largest differences, up to 20%. As well as the biases towards higher concentrations from the $V_{\rm max}$ method discussed above, another cause of differences is the fact that for an Einasto profile the conversion between $V_{\rm max}/V_{200}$ and c depends not only on c (as is the case for an NFW profile) but also on the Einasto shape parameter, α, with higher α giving higher $V_{\rm max}/V_{200}$. As is known (Gao et al. 2008) higher sigma haloes have higher α, which leads to an over-estimate of the halo concentration for high-σ haloes and an underestimate for low-σ haloes.

Klypin et al. (2011) and Prada et al. (2012) used velocity ratio method and found an upturn in the concentration mass relation for the highest mass haloes at all redshifts. As shown in Fig. 6, we recover an upturn at $z = 3$ when using $V_{\rm max}/V_{200}$ concentrations, but the relation is almost flat when using NFW concentrations, and has a negative slope when using Einasto concentrations. We suggest that the $V_{\rm max}/V_{200}$ method could be improved by assuming the Einasto profile with a mass dependent α as specified below in §6.

4 THE CONCENTRATION - MASS RELATION AT REDSHIFT ZERO

We start our analysis with the concentration mass relation at redshift zero. Here we use NFW fits to allow for better comparison with previous studies. In §6 we give the results for Einasto fits.

4.1 Planck vs WMAP

The concentration mass relations for relaxed haloes ($x_{\rm off} < 0.07$, $\rho_{\rm rms} < 0.5$) with more than 500 particles at redshift $z = 0$ in the Planck cosmology are shown in Fig. 7. The left panel shows the relation for our fiducial "virial" halo definition, while the right panel shows the relation for the $200\rho_{\rm crit}$ definition. The concentration mass relations are well fitted by a power-law:

$$\log_{10} c = a + b \log_{10}(M/[10^{12} h^{-1} {\rm M}_\odot]), \quad (7)$$

so that a is the zero point, and b is the slope. The best fit relations are shown by the solid red lines in Fig. 7 and are given by

$$\log_{10} c_{200} = 0.905 - 0.101 \log_{10}(M_{200}/[10^{12} h^{-1} {\rm M}_\odot]), \quad (8)$$

and

$$\log_{10} c_{\rm vir} = 1.025 - 0.097 \log_{10}(M_{\rm vir}/[10^{12} h^{-1} {\rm M}_\odot]). \quad (9)$$

The dotted, dashed and long-dashed lines show the corresponding relations for the WMAP 1st, 3rd and 5th year cosmologies (as presented in Macciò et al. 2008). For c_{200} the zero points were 0.917, 0.769, and 0.830, for the WMAP 1st, 3rd, and 5th year cosmologies, respectively. Note that for the virial halo definition (i.e., $M_{\rm vir}$) the virial overdensity is a function of the matter density, and thus varies between the different cosmologies. However, the $200\rho_{\rm crit}$ (i.e., M_{200}) definition is independent of cosmology, and thus the real cosmology induced structural differences are straight forward to see.

Our main result is that the concentrations in the Planck cosmology are $\sim 20\%$ higher than in the WMAP 5th year cosmology. Quite remarkably, the concentration mass relation in the Planck cosmology is very similar to that of the

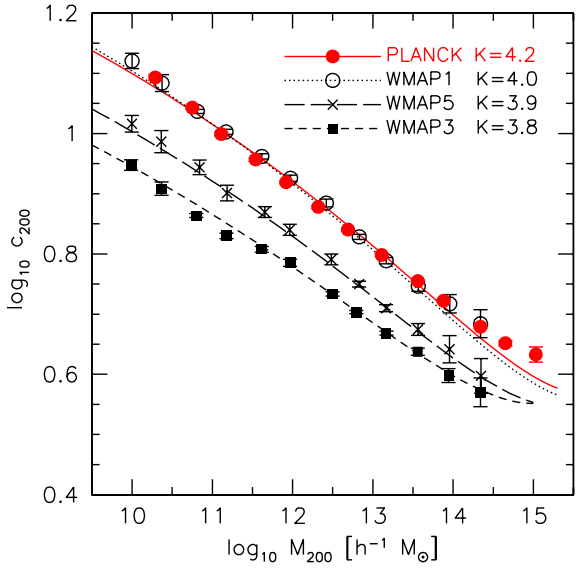

Figure 8. Comparison between concentration mass relations from simulations (symbols) with predictions from the analytic model of Bullock et al. (2001) as modified by Macciò et al. (2008). Note that the value of K needs to vary slightly (by up to 10%) to provide the best match to the simulations.

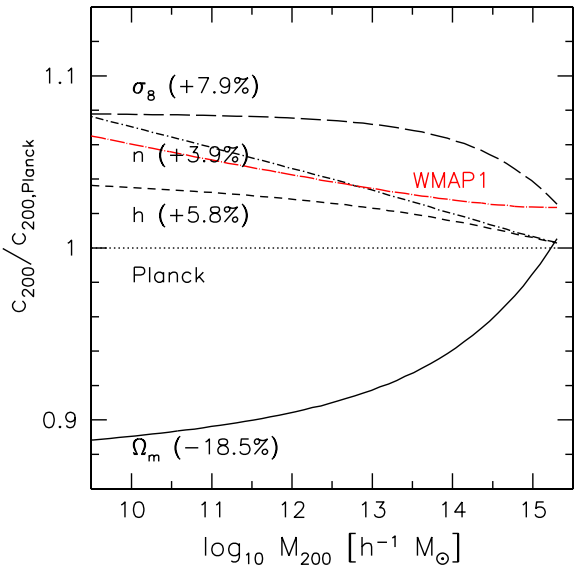

Figure 9. Effect of cosmological parameters on halo concentrations, relative to those from the Planck cosmology. This calculation was made using the model from Bullock et al. (2001). The various black lines show the effect of changing a single cosmological parameter from the Planck value to the WMAP1 value. The red line uses the WMAP1 parameters. This shows that higher σ_8, n, and h, are offset by a lower $\Omega_{\rm m}$.

WMAP 1st year cosmology, despite the significantly different cosmological parameters (see Table 1). In §4.2 below we show how the changes in the various cosmological parameters effect the concentration mass relation, and cancel each other out.

Finally, the distribution of concentrations around the mean concentration - mass relation is well described by a log-normal with an intrinsic scatter of 0.11 dex, consistent with results from different cosmologies (Macciò et al. 2008).

4.2 Comparison to analytic models

Fig. 8 shows the concentration mass relations for our simulations (symbols) compared to the analytic model of Bullock et al. (2001) as modified by Macciò et al. (2008). As found by Macciò et al. (2008), for this model to reproduce the simulations exactly, the parameter K needs to vary slightly (by a few percent) for different cosmologies. We find that $K \simeq 4.2$ provides the best match for the Planck cosmology. With the larger volumes for our simulations in the Planck cosmology we probe a factor of ~ 6 higher in halo mass, at these scales we see a departure from the Bullock model.

Given that the parameters are so different between the Planck and WMAP1 cosmologies: $\Omega_{\rm m} = 0.3175$ vs 0.268 (+18.5%); $h = 0.671$ vs 0.71 (-5.5%); $\sigma_8 = 0.8344$ vs 0.90 (-7.3%); $n = 0.9624$ vs 1.0 (-3.8%), we ask why are the Planck and WMAP1 concentration mass relations so similar? Fig. 9 shows the effect on halo concentrations (relative to the Planck cosmology) by chaining various cosmological parameters. Reducing the matter density ($\Omega_{\rm m}$) reduces the concentrations, while increasing the Hubble parameter (h), power spectrum normalization (σ_8), and power spectrum slope (n) increases the concentrations. The changes roughly cancel out, leaving an expected net increase of $2-7\%$ (depending on halo mass). The differences in the relations from our simulations are slightly smaller, but of a similar amplitude.

Since the model of Bullock et al. (2001) provides a good description of the relative changes in halo concentrations for different cosmological parameters we can use the model to estimate the uncertainty on concentrations from uncertainties in the cosmological parameters. We use posterior chains for the base/planck_lowl model, publicly available from the Planck Collaboration. This model assumes a flat cosmology. We pass the values of $\Omega_{\rm m}$, H_0, σ_8, n, and $\Omega_{\rm b}h^2$ through the Bullock et al. (2001) model. The resulting scatter in c_{200} at a halo mass of $M_{200} = 10^{12}h^{-1}\,{\rm M}_\odot$ is just 0.015 dex, or 3.5%. As we saw above in §3.1 the systematic differences in measuring halo concentrations are often larger than this. Furthermore, the intrinsic scatter in halo concentrations is almost an order of magnitude larger. Thus uncertainties cosmological parameters no longer are a significant source of systematic uncertainty in the prediction of concentrations of baryon free cold dark matter haloes.

5 EVOLUTION OF NFW CONCENTRATIONS

The evolution of the concentration mass relation for NFW fits is shown in Fig. 10. Upper panels show c_{200} vs M_{200}, while lower panels show $c_{\rm vir}$ vs $M_{\rm vir}$. The left hand panels show the median concentration mass relations from redshifts $z = 5$ to $z = 0$. At all redshifts the relations are well fitted by a power-law, except at the very highest masses, where there is some evidence for a departure from a power-law – specifically a flattening and sometimes an upturn in the median concentration (see also Klypin et al. 2011;

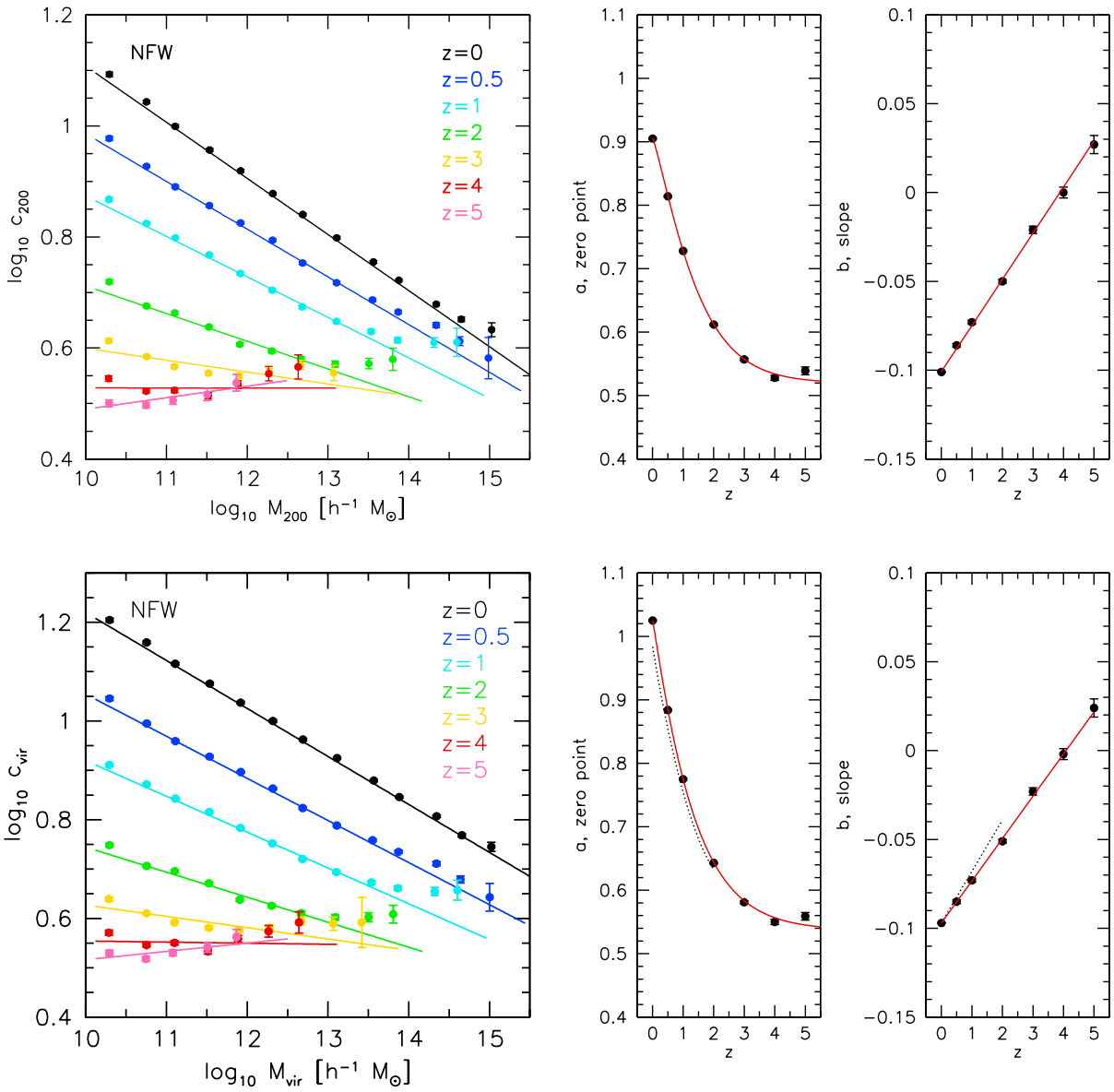

Figure 10. Evolution of the concentration mass relation using NFW fits. Upper panels show results for $c_{200} = R_{200}/r_{-2}$, while lower panels show results for $c_{\rm vir} = R_{\rm vir}/r_{-2}$. The left panels show the median concentration in bins of halo mass from redshifts $z = 0$ to $z = 5$ (with colors as indicated). The solid lines are power-law fits of the form $\log_{10} c = a + b \log_{10}(M/10^{12} h^{-1}\,{\rm M}_\odot)$. The parameters of these fits are given as black points in the right panels, with the error bars showing 1σ uncertainties. The evolution of the slope is linear with redshift, while the evolution of the zero point is approximately exponential with redshift. The red solid lines give fitting formula for the evolution (see Eqs. 10-13). For reference, the dotted lines give the evolution (from $z = 0$ to $z = 2$) in the WMAP5 cosmology from Muñoz-Cuartas et al. (2011).

Prada et al. 2012). However, as we discuss above in §3.1, the size of this departure is dependent on the method used to measure halo concentrations: e.g., NFW fits, Einasto fits, $V_{\rm max}/V_{200}$. The $V_{\rm max}$ method results in the largest up-turn, while Einasto fits show no evidence for an up-turn. Additionally, as shown by Ludlow et al. (2012) the use of $V_{\rm max}/V_{200}$ as a concentration estimator is especially sensitive to transient features due to unrelaxed haloes. We thus caution against over-interpretation of this feature.

The panels on the right show the evolution of the slope and normalization of the concentration mass relation fitted using Eq. 7. The slope changes linearly with redshift, while the zero point approaches a constant value above $z \sim 3$. The data for the slopes and zero points are given in Table 3. Fits to the evolution of the slope and zero points are shown with solid red lines. For the c_{200} vs M_{200} relation these are given by

$$b = -0.101 + 0.026z \tag{10}$$

$$a = 0.520 + (0.905 - 0.520)\exp(-0.617z^{1.21}), \tag{11}$$

and for the $c_{\rm vir}$ vs $M_{\rm vir}$ relation by

$$b = -0.097 + 0.024z \tag{12}$$

Table 3. Fit parameters for the concentration mass relation: $\log_{10} c = a + b \log_{10}(M/[10^{12} h^{-1} \mathrm{M}_\odot])$.

Profile	Δ	Redshift	zero point (a)	slope (b)
NFW	200	0.0	0.905 ±0.001	-0.101 ±0.001
NFW	200	0.5	0.814 ±0.001	-0.086 ±0.001
NFW	200	1.0	0.728 ±0.001	-0.073 ±0.001
NFW	200	2.0	0.612 ±0.001	-0.050 ±0.001
NFW	200	3.0	0.557 ±0.003	-0.021 ±0.002
NFW	200	4.0	0.528 ±0.004	0.000 ±0.003
NFW	200	5.0	0.539 ±0.006	0.027 ±0.005
NFW	104.2	0.0	1.025 ±0.001	-0.097 ±0.001
NFW	138.4	0.5	0.884 ±0.001	-0.085 ±0.001
NFW	156.9	1.0	0.775 ±0.001	-0.073 ±0.001
NFW	170.6	2.0	0.643 ±0.001	-0.051 ±0.001
NFW	174.5	3.0	0.581 ±0.002	-0.023 ±0.002
NFW	176.0	4.0	0.550 ±0.004	-0.002 ±0.003
NFW	177.3	5.0	0.559 ±0.006	0.024 ±0.005
Einasto	200	0.0	0.978 ±0.006	-0.125 ±0.004
Einasto	200	0.5	0.884 ±0.005	-0.117 ±0.004
Einasto	200	1.0	0.775 ±0.004	-0.100 ±0.004
Einasto	200	2.0	0.613 ±0.004	-0.073 ±0.006
Einasto	200	3.0	0.533 ±0.005	-0.027 ±0.009
Einasto	200	4.0	0.481 ±0.009	-0.020 ±0.014
Einasto	200	5.0	0.478 ±0.022	0.013 ±0.032

$$a = 0.537 + (1.025 - 0.537)\exp(-0.718 z^{1.08}). \quad (13)$$

For comparison purposes the fitting formula (from $z = 2$ to $z = 0$) for the $c_{\rm vir} - M_{\rm vir}$ relation in the WMAP5 cosmology form Muñoz-Cuartas et al. (2011) is given by dotted lines. The form of the evolution in slope and zero point is qualitatively the same, although the details differ.

5.1 Comparison with analytic models

A comparison between the results of our N-body simulations and predictions of several analytic models are shown in Fig. 11. The upper left panel shows our fitting formula (Eqs. 10 & 11). The upper right panel shows the Navarro, Frenk, & White (1997) model using the original parameters $F = 0.5$, $f = 0.01$, $C = 3000$. The success of this model is in reproducing the concentrations of massive $M_{200} \gtrsim 10^{13} h^{-1}\,\mathrm{M}_\odot$ haloes at redshift $z = 0$. At all other masses and redshifts, however, this model does a poor job at reproducing our simulation results. Specifically it predicts much weaker evolution in the slope and zero point than our simulations (see also Bullock et al. 2001).

The lower left panel shows the Bullock et al. (2001) model as modified by Macciò et al. (2008). As in Fig. 8 we use $K = 4.2$. The success of this model is in reproducing the slope of the concentration mass relation for low mass haloes at all redshifts. It also does quite well in reproducing the zero point evolution. The model fails in reproducing the concentrations of high mass haloes. An approximate solution to this problem is to set the concentration to the parameter K at redshifts before the collapse time of the halo.

The lower right panel shows the Zhao et al. (2009) model. Overall, this fares better than both the NFW and Bullock models, but not as well as our fitting formula. Note that in the Zhao et al. (2009) model there is a minimum concentration of $c_{\rm vir} = 4$. Since the ratio between $c_{\rm vir}/c_{200}$ increases towards lower redshifts, this results in their model predicting the lowest c_{200} in the highest mass haloes at $z = 0$. We have verified that their model still under predicts the concentrations of high mass haloes at low redshifts when we plot $c_{\rm vir}$ vs $M_{\rm vir}$.

6 EVOLUTION OF EINASTO PARAMETERS

In this section we discuss the evolution of structural parameters from Einasto fits to dark matter haloes: scale radii as expressed through the concentration parameter, c, and the Einasto shape parameter, α. These provide a more accurate description of CDM halo profiles than the NFW function (see § 3), and thus should be used whenever possible. Recall, as discussed in section 2.4, in order to recover robust parameters we require more particles for Einasto fits than for NFW ones, and more particles for lower redshift haloes. This results in redshift dependent lower halo mass limits.

6.1 Concentration mass relation

Fig. 12 shows the evolution of the concentration mass relation obtained from Einasto fits, and using the $\Delta = 200$ halo definition. The evolution of the slope and zero point is given by

$$b = -0.130 + 0.029 z, \quad (14)$$

$$a = 0.459 + (0.977 - 0.459)\exp(-0.490 z^{1.303}). \quad (15)$$

The slope evolution is consistent with being linear in redshift, which implies a positive slope at $z > 4.5$. Our measurement at $z = 5$ is consistent with the linear evolution, but also, within the errors with a slope of zero. Further work is needed to constrain the behaviour of the slope evolution at very high redshift. For comparison, the green points in the right hand panels of Fig. 12 show results from $z = 2$ to $z = 0$ from Gao et al. (2008) who used the Millennium Simulation. Their results have a very similar zero point evolution as ours, but a stronger slope evolution.

6.2 Einasto shape parameter

The upper panel of Fig. 13 shows the evolution of the Einasto shape parameter, α, as a function of halo mass. At low redshifts a Milky Way mass halo ($M_{200} \sim 10^{12} h^{-1}\,\mathrm{M}_\odot$) has on average $\alpha \simeq 0.16$, which is consistent with results from much higher resolution simulations of individual haloes (Navarro et al. 2010). At higher masses α increases gradually until $M_{200} \sim 10^{14} h^{-1}\,\mathrm{M}_\odot$, above which α increases rapidly. This mass dependence qualitatively explains the differences between inner density profile slopes obtained from NFW and Einasto fits in Fig. 2. From Fig. 3 we expect haloes to be denser than NFW at small radii, with a larger difference at lower masses – which is exactly what we find in Fig. 2.

The mass dependence of the Einasto shape parameter is present at all redshifts we probe. At fixed halo mass α increases with redshift, such that at redshift $z \sim 4$ haloes of Milky Way mass have $\alpha \simeq 0.25$. As shown by Gao et al. (2008) this evolution effectively disappears when the

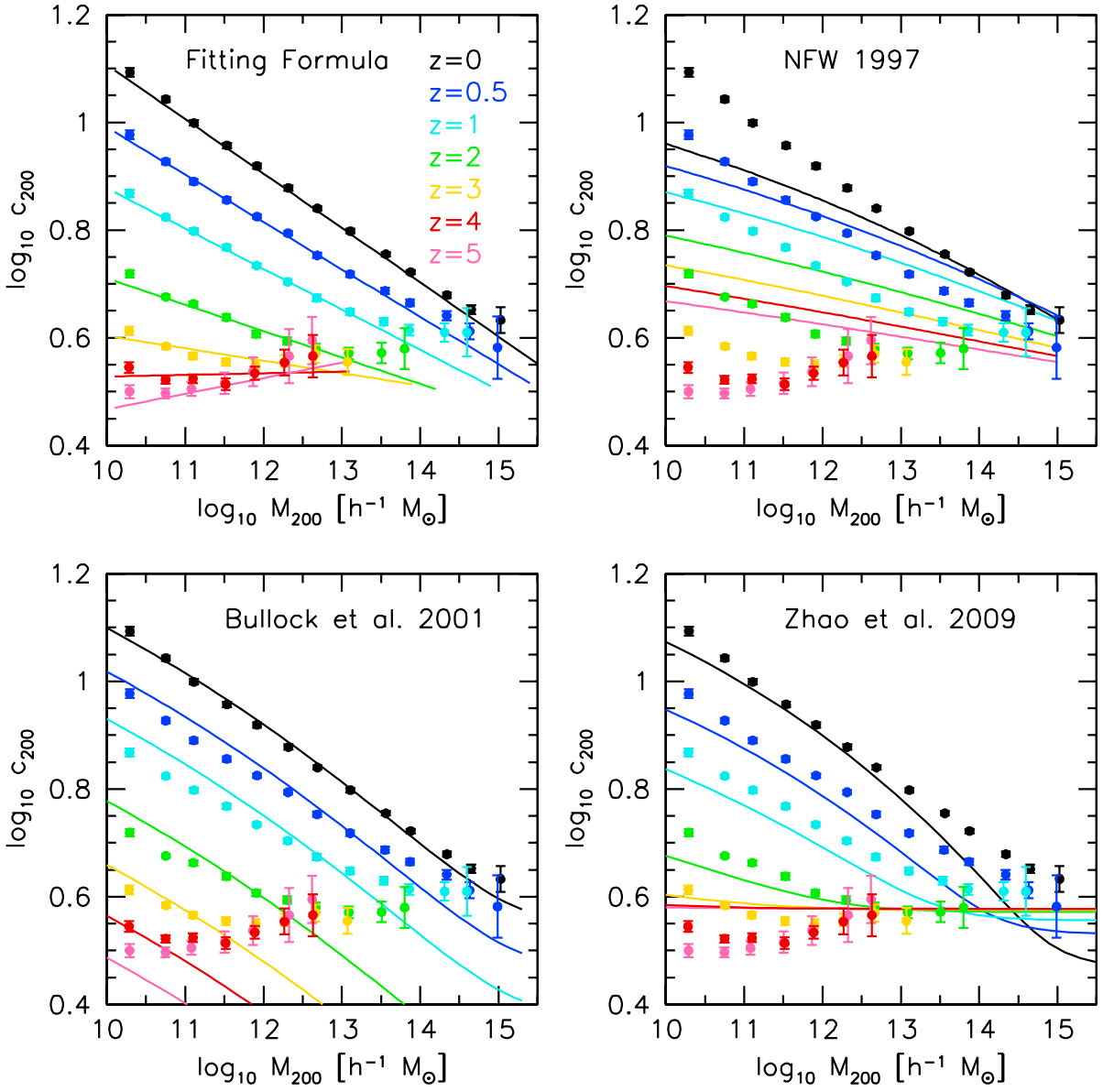

Figure 11. Comparison between concentration mass relations from simulations at redshifts $z = 0$ to $z = 5$ (points and errors on the median) with our fitting formula (upper left) together with predictions from the analytic models of Navarro, Frenk, & white (1997); Bullock et al. (2001); and Zhao et al. (2009).

halo virial mass is replaced by the dimensionless peak height, $\nu(M, z)$:

$$\nu(M, z) = \delta_{\rm crit}(z)/\sigma(M, z). \quad (16)$$

Where $\delta_{\rm crit}(z)$ is the ratio of the linear density threshold for collapse at redshift z, and $\sigma(M, z)$ is the rms linear density fluctuation at z within spheres of mean enclosed mass, M. The parameter $\nu(M, z)$ is related to the abundance of objects of mass M at redshift z. The characteristic mass $M_*(z)$ of the halo mass distribution at redshift z is defined through $\nu(M_*, z) = 1$.

In the lower panel in Fig. 13 we confirm this result and extend it to higher redshifts (the highest redshift analyzed by Gao et al. 2008 was $z = 3$). The dotted line shows the relation between α and ν from Gao et al. (2008) and is given by

$$\alpha = 0.0095\nu^2 + 0.155. \quad (17)$$

This provides a good match to our simulation results, even though the cosmological parameters are significantly different. The dotted lines in the upper panel of Fig. 13 show the predicted α vs M_{200} relation from Eq. 17. Since these relations require a numerical calculation, in Appendix A we provide accurate fitting formulae for calculating the $\nu(M, z)$.

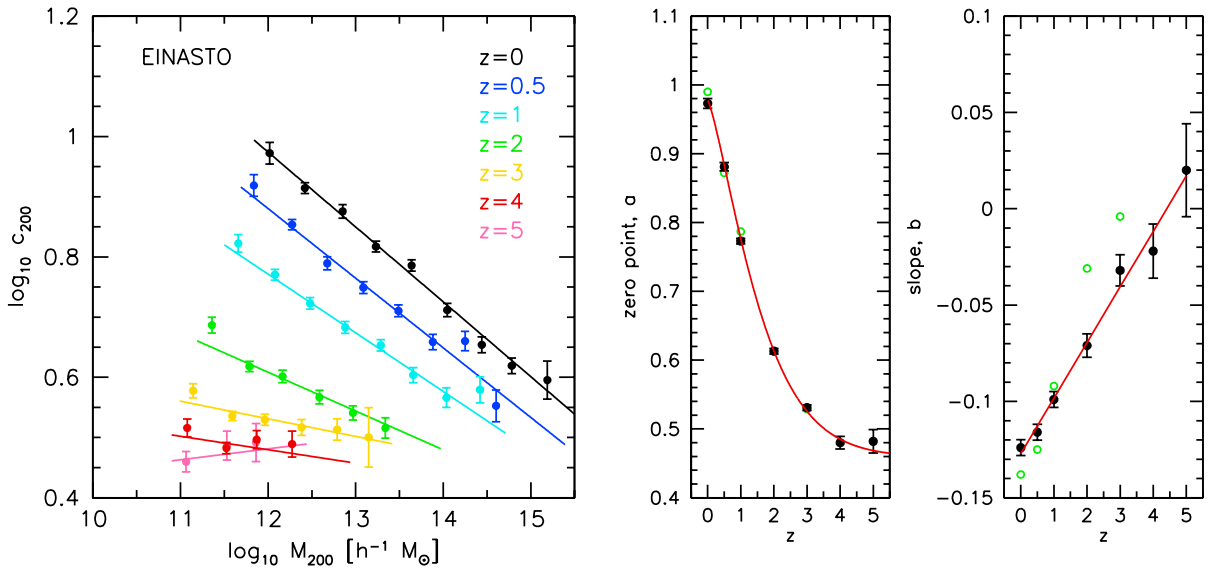

Figure 12. Evolution of the concentration mass relation using Einasto fits and the $c_{200} = R_{200}/r_{-2}$ definition. The left panels show the median concentration in bins of halo mass from redshifts $z = 0$ to $z = 5$ (with colors as indicated). The solid lines are power-law fits of the form $\log_{10} c_{200} = a + b \log_{10}(M_{200}/10^{12} h^{-1}\,\mathrm{M}_\odot)$. The parameters of these fits are given as black points in the right panels, with the error bars showing 1σ uncertainties. As with the NFW concentrations (Fig. 10) the evolution of the slope is linear with redshift, while the evolution of the zero point is approximately exponential with redshift. The red solid lines give fitting formula for the evolution (see Eqs. 14 & 15). The green open circles show results from Gao et al. (2008) for the WMAP1 cosmology (for redshifts $z = 0$ to $z = 3$), who find a similar zero point evolution, but stronger slope evolution.

6.3 Concentration vs peak height

The concentration vs halo mass relation evolves strongly. However, as shown by previous authors (Prada et al. 2012; Ludlow et al. 2013b) there is much less evolution when the halo mass is replaced by the dimensionless peak height parameter, $\nu(M, z)$.

Using the set of Millennium Simulations (which assume a cosmology similar to WMAP1) Ludlow et al. (2013b) argue that the $c_{200} - \nu$ relation has no redshift dependence (since $z = 2$). They use this as a basis for an analytic model for the evolution of halo concentrations. Using a wider range of simulations and cosmologies, Prada et al. (2012) find significant redshift dependence (since $z = 10$). Fig. 14 shows the evolution of the concentration vs peak height relation from redshifts $z = 5$ to $z = 0$ from our simulations. In agreement with Prada et al. (2012), but in disagreement with Ludlow et al. (2013), we find that this relation is not redshift independent. For example, at $\nu = 2$ (i.e., a 2σ mass fluctuation) we find a factor of 1.6 increase in concentration from $z = 4$ to $z = 0$, which is much larger than can be attributed to systematic errors in measuring halo concentrations.

In light of the redshift independent relation between Einasto shape parameter, α, and ν it is natural to ask whether R_{200}/r_{-2} is the correct way to define halo concentrations. Note that other commonly used definitions of the virial radius, will only result in more evolution. For example, at redshift zero $c_{\rm vir}/c_{200} \sim 1.3$, while at high redshift $c_{\rm vir}/c_{200} \sim 1$.

6.4 Scatter in structural parameters

Gao et al. (2008) fitted Einasto profiles to stacks of haloes in bins of halo mass. Here, we fit Einasto profiles to individual haloes, and thus can measure the scatter in α. The distribution of $\alpha(\nu)$ and $c(M)$ are shown in Fig. 15. Both distributions are well described by log-normal functions. For c the standard deviation is roughly independent of redshift at 0.13 dex. For α the measured standard deviation increases with redshift roughly following $\sigma_{\log_{10}\alpha} = 0.16 + 0.03z$. Thus the halo mass and redshift, or equivalently the peak height parameter, are not sufficient to fully specify the structure of CDM haloes.

One must be wary of covariances between parameters when fitting Einasto profiles. For example, Ludlow et al. (2013a) showed that at fixed halo mass α and concentration are negatively correlated – haloes with higher fitted α have lower concentration. We also find such a correlation when using Einasto fit parameters. However when using NFW concentrations and Einasto α there is very little correlation. Thus at this stage we do not wish to over-interpret the amount of scatter in α, nor its correlation with the concentration parameter.

7 COMPARISON WITH OBSERVATIONS

In Fig. 16 we compare the concentration mass relation from our simulations with observational measurements, both using NFW fits. The points show a sampling of individual haloes from our simulations at redshift $z = 0$. The solid black

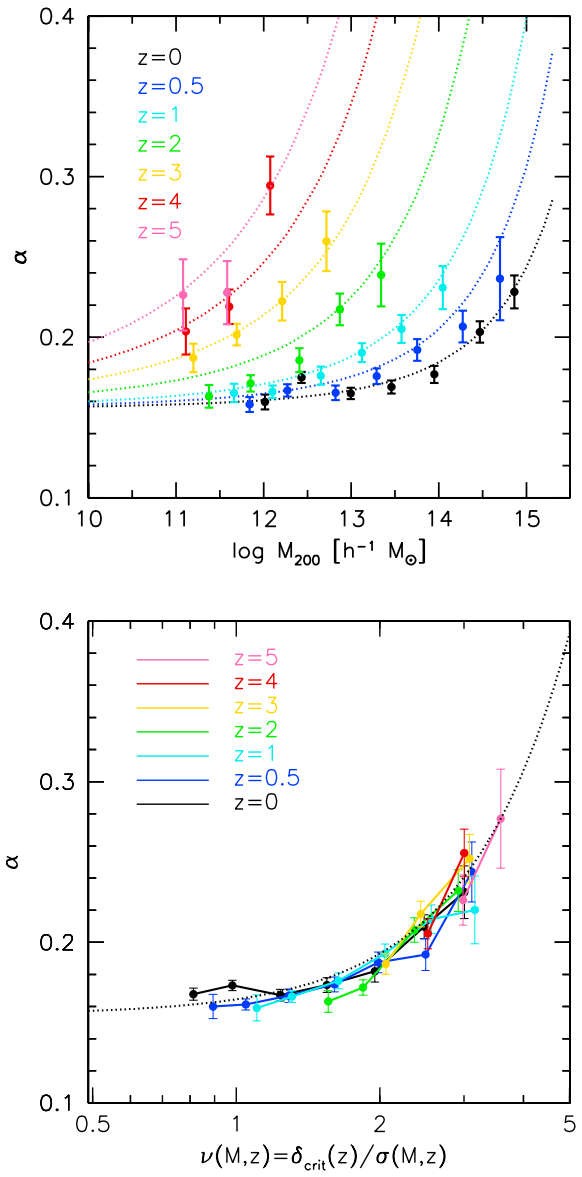

Figure 13. Evolution of median Einasto shape parameter, α, versus halo mass (upper panel) and dimensionless peak height parameter $\nu(M,z) = \delta_{\rm crit}(z)/\sigma(M,z)$ (lower panel). The dotted lines are the relation from Gao et al. (2008), which also provides a good fit to our simulation data in spite of the different cosmological parameters.

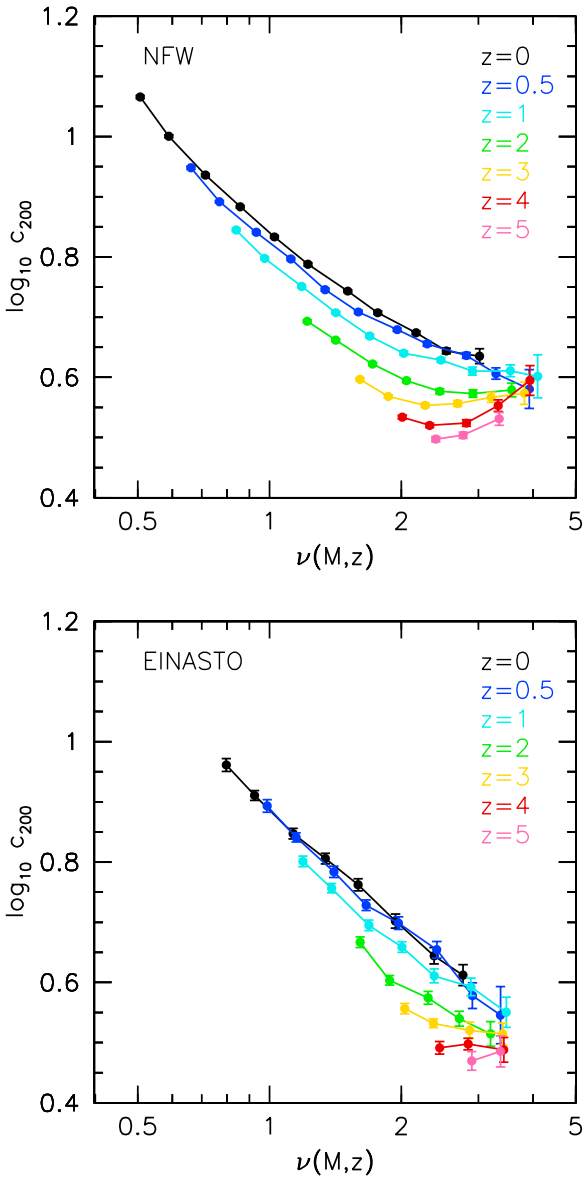

Figure 14. Evolution of median concentration parameter, $c_{200} = R_{200}/r_{-2}$ as a function of dimensionless peak height parameter $\nu(M,z)$ for NFW fits to haloes with more than 500 particles (upper panels) and Einasto fits to haloes with $N_{\rm min}$ as describe in §2.4 (lower panels). In contrast to the relation between Einasto shape parameter and halo mass (Fig. 13), the evolution in the concentration mass relation is not removed when replacing halo mass with peak height parameter.

line shows our fitting formula for NFW profiles, with the dotted lines showing $\pm1\sigma$ scatter. The blue long-dashed and red short-dashed lines show the corresponding relations for $z = 0.2$ and $z = 0.4$, respectively. The black pentagons show observational results for spiral galaxies at redshift $z \simeq 0$ from the DiskMass project (Bershady et al. 2010; Martinsson et al. 2013). The blue circles show results for x-ray luminous clusters at redshifts $z = 0.1$ to 0.3 from Ettori et al. (2010). The red square shows the mean mass and concentration from an analysis of strong lensing groups and clusters by Auger et al. (2013), which have a mean redshift of $z \simeq 0.4$. Recall the uncertainty on cosmological parameters imparts just a 3.5% uncertainty to the concentrations of Milky Way mass haloes, which is much smaller than the systematic measurement uncertainties in both observation and theory.

Individually, the results from spirals and clusters imply a very steep slope to the concentration mass relation. However, as shown by Auger et al. (2013), the steep slope is almost entirely due to the covariance between halo mass and concentration. This can also be seen in the x-ray cluster data from Ettori et al. (2010), since the authors use two methods to estimate halo masses and concentrations. In Fig. 16 the

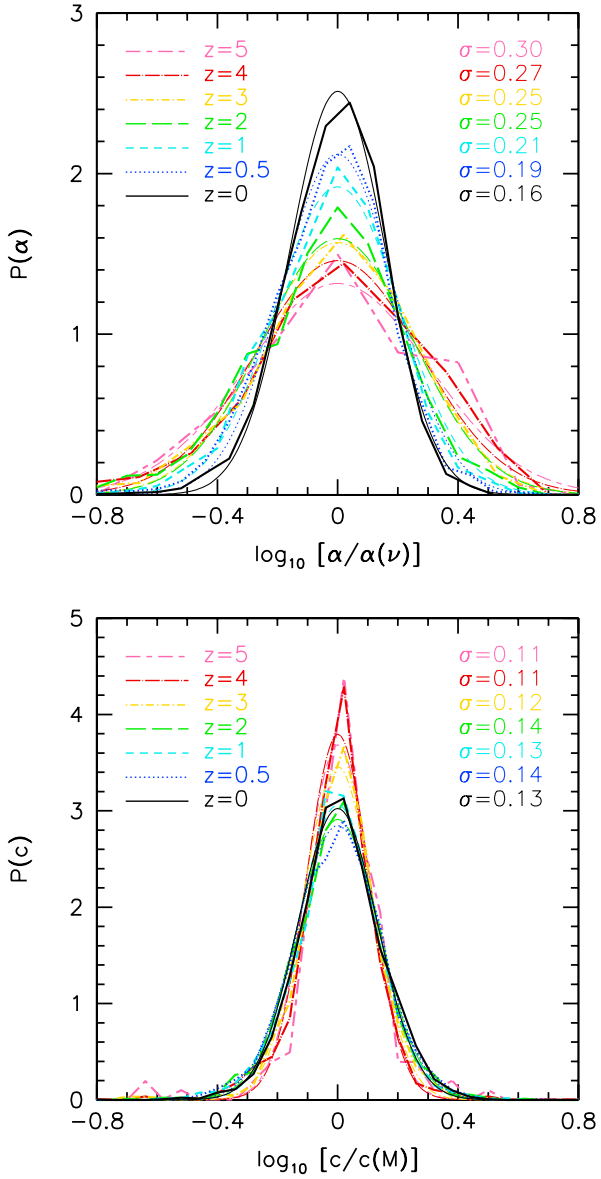

Figure 15. Scatter in the Einasto concentration, c, and shape parameter, α, as a function of redshift. The distributions of c and α are well described by log-normals with scatter of ~ 0.13 dex and ~ 0.2 dex, respectively.

two numbers for each cluster are connected by a diagonal line, which has a mean slope of -0.82.

The median concentrations and masses for the spirals and x-ray clusters are shown with a solid pentagon and solid circle, respectively. Together these imply a slope to the observed concentration mass relation of $\simeq -0.1$. In addition, since both points are close to the median concentration-mass relations from our simulations, this suggests that dark matter haloes have, on average, experienced little response to galaxy formation. While there are several caveats in directly interpreting this plot, it shows that the ΛCDM paradigm is consistent with the observations of massive dark matter haloes.

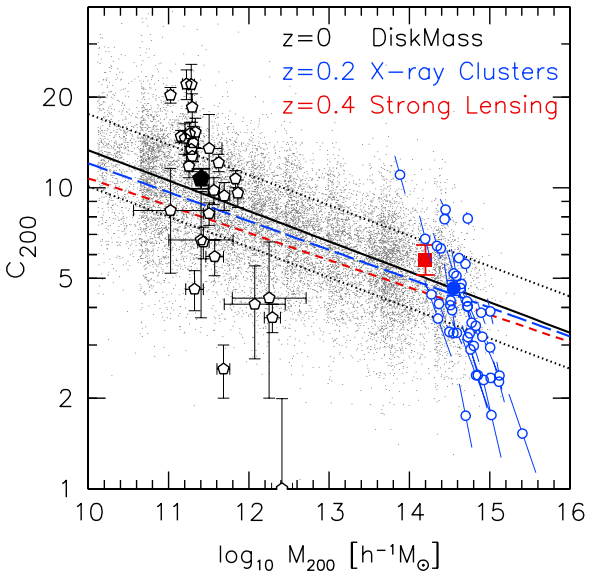

Figure 16. Comparison between the NFW concentration mass relation from our simulations (lines and points) with observations of spiral galaxies (black pentagons) and clusters of galaxies (blue circles, red square). For each cluster there are two measurements. We plot the average and connect the two measurements with a line. This demonstrates the fitting degeneracy between concentration and halo mass. For the spirals and clusters the filled symbols shows the median concentration and halo mass. Combining the observational data sets yields a slope and zero point in good agreement with our simulations, implying only mild halo response at these two scales.

8 SUMMARY

In this paper we have used a large set of cosmological N-body simulations to study the evolution of the structure of cold dark matter haloes over 90% of the age of the Universe. At redshift zero our simulations span five orders of magnitude in halo mass ($10^{10}-10^{15}h^{-1}\,\mathrm{M}_\odot$), covering haloes those that host individual dwarf galaxies to those associated with massive clusters. We adopt the cosmological parameters derived from the first data release of the Planck Satellite (the Planck Collaboration 2013). We summarize our results as follows:

- The concentration mass relation in the Planck cosmology has a 20% higher normalization (at redshift $z = 0$) than in the WMAP 5th year cosmology. Despite significant differences in cosmological parameters the Planck concentration mass relation is very similar to that from the WMAP1 cosmology. By coincidence, the increased Ω_m (in the Planck vs WMAP1 cosmology) is almost perfectly balanced by the decrease in σ_8, n, and h.
- Propagating the uncertainties in cosmological parameters given by the Planck Collaboration results in just a 3.5% uncertainty in the concentrations of Milky Way mass haloes at redshift $z = 0$, which is smaller than typical systematic uncertainties in measuring halo concentrations.
- In agreement with previous studies we find that the spherically averaged density profiles of CDM haloes are better described by the Einasto (1965) profile than the NFW (1997) profile. For example, between 2% and 4% of the virial

radius, simulated haloes of mass $M_{200} \sim 10^{13} h^{-1}\,\mathrm{M}_\odot$ (which host massive elliptical galaxies) have average logarithmic density slopes $d\log\rho/d\log r \simeq -1.6$, compared to $\simeq -1.4$ for NFW fits.

- At fixed redshift the average Einasto shape parameter, α, increases with halo mass, from $\alpha \sim 0.16$ for dwarf haloes to $\alpha \sim 0.25$ for cluster haloes. At fixed halo mass the average, α, increases systematically with redshift. This evolution is well described by the relation between α and dimensionless peak height $\nu(M,z) = \delta_{\rm crit}(z)/\sigma(M,z)$ proposed by Gao et al. (2008) — who used the WMAP1 cosmology.
- The distribution in α about the $\alpha-\nu$ relation is well described by a log-normal function, with a standard deviation in $\log_{10}\alpha$ of ~ 0.2 and a slight dependence on redshift.
- We find systematic differences of up to $\sim 10\%$ in halo concentrations due to different fitting methods. Relative to Einasto fits the $V_{\rm max}/V_{200}$ method (e.g., Klypin et al. 2011; Prada et al. 2012) gives systematically higher concentrations (by up to 20%) at higher masses and higher redshifts. A consequence of these systematic differences is the upturn in the concentration mass relation at high masses and redshifts (e.g., Klypin et al. 2011; Prada et al. 2012) is not present for our Einasto fits.
- None of the analytic models in the literature (e.g., NFW 1997; Bullock et al. 2001; Zhao et al. 2009) accurately reproduce the evolution of the concentration mass relation. We provide simple fitting formulae for NFW (Eqs. 10-13) and Einasto fits (Eqs. 14 & 15), which are valid between redshifts $z = 5$ and $z = 0$.
- The observed concentrations and halo masses from NFW fits to data of spiral galaxies from the DiskMass project (Bershady et al. 2010; Martinsson et al. 2013), groups and clusters of galaxies (Ettori et al. 2010; Auger et al. 2013) are in good agreement with our simulations suggesting only mild halo response on these scales.

ACKNOWLEDGEMENTS

We acknowledge support from the Sonderforschungsbereich SFB 881 "The Milky Way System" (subproject A1) of the German Research Foundation (DFG). The numerical simulations were performed on the *theo* supercomputer at the Max-Planck-Institut für Astronomie at the Rechenzentrum in Garching, and on the *Milky Way* supercomputer, co-funded by SFB 881 (subproject Z2) and by the Jülich Supercomputing Center (JSC).

REFERENCES

Auger, M. W., Budzynski, J. M., Belokurov, V., Koposov, S. E., & McCarthy, I. G. 2013, MNRAS, 2217
Bershady, M. A., Verheijen, M. A. W., Swaters, R. A., et al. 2010, ApJ, 716, 198
Bertschinger E. 2001, ApJS, 137, 1
Bullock J. S., Kolatt T. S., Sigad Y., Somerville R. S., Kravtsov A. V., Klypin A. A., Primack J. R., Dekel A. 2001, MNRAS, 321, 559 (B01)
de Blok, W. J. G., McGaugh, S. S., Bosma, A., & Rubin, V. C. 2001, ApJL, 552, L23
Di Cintio, A., Brook, C. B., Macciò, A. V., et al. 2014, MNRAS, 437, 415
Duffy, A. R., Schaye, J., Kay, S. T., & Dalla Vecchia, C. 2008, MNRAS, 390, L64
Dutton, A. A., van den Bosch, F. C., Dekel, A., & Courteau, S. 2007, ApJ, 654, 27
Einasto, J. 1965, Trudy Astrofizicheskogo Instituta Alma-Ata, 5, 87
Eke, V. R., Navarro, J. F., & Steinmetz, M. 2001, ApJ, 554, 114
Ettori, S., Gastaldello, F., Leccardi, A., et al. 2010, A&A, 524, A68
Flores, R. A., & Primack, J. R. 1994, ApJL, 427, L1
Gao, L., Navarro, J. F., Cole, S., et al. 2008, MNRAS, 387, 536
Klypin, A. A., Trujillo-Gomez, S., & Primack, J. 2011, ApJ, 740, 102
Komatsu, E., Dunkley, J., Nolta, M. R., et al. 2009, ApJS, 180, 330
Ludlow, A. D., Navarro, J. F., Li, M., et al. 2012, MNRAS, 427, 1322
Ludlow, A. D., Navarro, J. F., Boylan-Kolchin, M., et al. 2013a, MNRAS, 432, 1103
Ludlow, A. D., Navarro, J. F., Angulo, R. E., et al. 2013b, arXiv:1312.0945
Macciò A. V., Dutton A. A., van den Bosch F. C., Moore B., Potter D., Stadel J. 2007, MNRAS, 378, 55
Macciò, A. V., Dutton, A. A., & van den Bosch, F. C. 2008, MNRAS, 391, 1940
Martinsson, T. P. K., Verheijen, M. A. W., Westfall, K. B., et al. 2013, A&A, 557, A131
McGaugh, S. S. 2004, ApJ, 609, 652
Merritt, D., Navarro, J. F., Ludlow, A., & Jenkins, A. 2005, ApJL, 624, L85
Merritt, D., Graham, A. W., Moore, B., Diemand, J., & Terzić, B. 2006, AJ, 132, 2685
Mo, H. J., Mao, S., & White, S. D. M. 1998, MNRAS, 295, 319
Moore, B. 1994, Nature, 370, 629
Muñoz-Cuartas, J. C., Macciò, A. V., Gottlöber, S., & Dutton, A. A. 2011, MNRAS, 411, 584
Mainini R., Macciò A. V., Bonometto S. A., Klypin A. 2003, ApJ, 599, 24
Navarro J. F., Frenk C. S., White S. D. M. 1996, ApJ, 462, 563
Navarro J. F., Frenk C. S., White S. D. M. 1997, ApJ, 490, 493 (NFW)
Navarro, J. F., Hayashi, E., Power, C., et al. 2004, MNRAS, 349, 1039
Navarro, J. F., Ludlow, A., Springel, V., et al. 2010, MNRAS, 402, 21
Planck Collaboration, Ade, P. A. R., Aghanim, N., et al. 2013, arXiv:1303.5076
Power, C., Navarro, J. F., Jenkins, A., et al. 2003, MNRAS, 338, 14
Prada, F., Klypin, A. A., Cuesta, A. J., Betancort-Rijo, J. E., & Primack, J. 2012, MNRAS, 423, 3018
Reed, D. S., Koushiappas, S. M., & Gao, L. 2011, MNRAS, 415, 3177
Spergel D. N., et al. 2003, ApJS, 148, 175
Spergel D. N., et al. 2007, ApJS, 170, 377
Springel V., et al. 2005, Nature, 435, 629

Stadel J. G. 2001, Ph.D. Thesis, University of Washington
Stadel, J., Potter, D., Moore, B., et al. 2009, MNRAS, 398, L21
Zentner, A. R., & Bullock, J. S. 2002, Phy.Rev.D, 66, 043003
Zhao D. H., Mo H. J., Jing Y. P., Börner, G. 2003a, MNRAS, 339, 12
Zhao, D. H., Jing, Y. P., Mo, H. J., Börner, G. 2009, ApJ, 707, 354

APPENDIX A: PEAK HEIGHT VS HALO MASS AND REDSHIFT

The relation between halo mass, M, and dimensionless peak height parameter, $\nu(M,z) = \delta_{\rm crit}(z)/\sigma(M,z)$, requires a numerical calculation. For convenience here we provide a fitting formula for the relation between halo mass, peak height and redshift. Since the redshift dependence of $\nu(M,z)$ is independent of halo mass, we split the relation into two parts:$\nu(M,z) = \nu(M,0) \times [\nu(M,z)/\nu(M,0)]$.

The relation between peak height and halo mass at redshift zero is shown in Fig. A1 and is approximated by

$$\log_{10}\nu = -0.11 + 0.146m + 0.0138m^2 + 0.00123m^3 \quad \text{(A1)}$$

where $m = \log_{10}(M_{200}/10^{12}h^{-1}\,{\rm M}_\odot)$. As shown in the lower panel of Fig. A1 this approximation reproduces the numerical calculation to better than 1% for halo masses $10^9 \lesssim M_{200}/[h^{-1}\,{\rm M}_\odot] \lesssim 10^{15}$. The redshift evolution of ν is shown in Fig. A2 and is approximated by

$$\frac{\nu(M,z)}{\nu(M,0)} = 0.033 + 0.79(1+z) + 0.176\exp(-1.356z), \quad \text{(A2)}$$

and is accurate to better than 0.1% for redshifts $0 < z < 5$. Note that the evolution at high redshift is linear since $\Omega_{\rm m}(z) \to 1$. The deviation from a linear relation at low redshifts is due to the increased contribution of Ω_Λ.

Together with Eq. 17, Eqs. A1 & A2 can be used to calculate the redshift dependence of the average Einasto shape parameter as a function of halo mass.

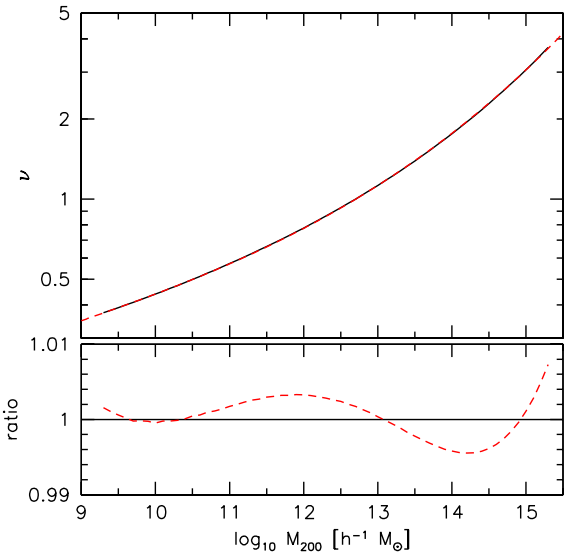

Figure A1. Relation between dimensionless peak height, ν, and halo mass, M_{200} (upper panel). The black solid line shows the numerical calculation while the red dashed line shows our fitting formula Eq. A1, which is accurate to better than 1% for the mass range plotted (lower panel).

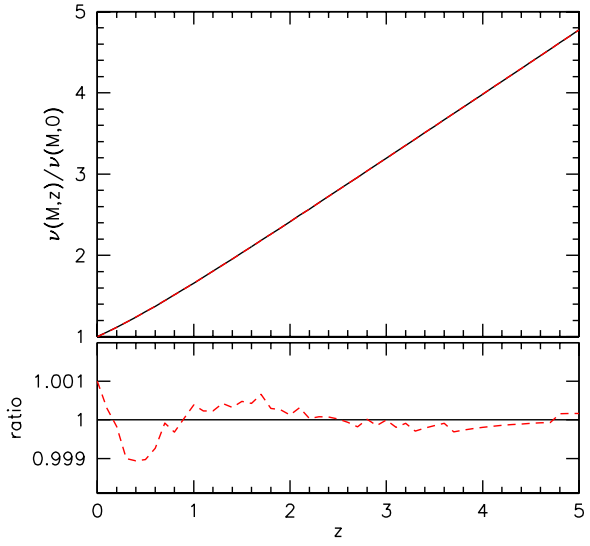

Figure A2. Evolution of dimensionless peak height, ν (upper panel). The black solid line shows the numerical calculation while the red dashed line shows our fitting formula Eq. A2, which is accurate to better than 0.1% for the redshift range shown (lower panel).